ChemComm

Check for updates

Upcycling of spent LiCoO₂: engineering the coordination-trapping behavior towards conversion-type anodes for advanced Li-storage†

Zihao Zeng,‡ Hai Lei,‡ Yunpeng Wen, Chao Zhu, Jiexiang Li, Wei Sun, [ID]
Yue Yang [ID] and Peng Ge [ID]*

Based on its high economic/sustainability value, the upcycling of spent cathodes into anodes has been deemed to be an alternative strategy to traditional chemical synthesis. Supported by an effective acid leaching and coordination-trapping self-assembly reaction, a nano-scale CoS@NSC anode was successfully prepared from spent LiCoO₂ and used as a promising anode for lithium ion batteries.

Given their high specific capacity and extraordinary conductivity, transition metal sulfides have been deemed to be promising anodes for energy storage systems, including lithium ion batteries (LIBs), sodium ion batteries (SIBs), and others.[1–3] However, the large-scale production of metal sulfides suffers from the high cost of raw materials and cumbersome preparation process.[4–6] To solve the problems above, a series of studies have focused on natural minerals, proposing short-process mineral regeneration processes such as gas-phase melting methods, and achieving the fabrication of metal sulfides with improved Li/Na ion storage capabilities.[7–9] Compared to natural minerals, urban mineral resources, such as spent batteries, have captured greater attention due to their having higher metal enrichment and fewer impurities.[10–12] At present, hydrometallurgy, pyrometallurgy and direct regeneration methods have been utilized to recover the cathode materials of spent LIBs, accompanied by considerable advances.[13–15] Supported by the hydrometallurgy process, the metal ions could be recovered in the form of ions. Meanwhile, with the assistance of a flotation agent, the metal ions could be captured by the sulfhydryl group (–SH), leading to self-assembly into flotation agent–metal complexes.[16] Similar to metal organic frameworks (MOFs), the as-obtained complexes consisted of two parts: the hydrocarbon chains and the sulfhydryl group–metal part. Thus, inspired by the flotation chemistry and structure traits of MOFs, it was expected that the prepared complexes could be transformed into

School of Minerals Processing and Bioengineering, Central South University, Changsha 410083, China. E-mail: gp-gepeng@csu.edu.cn

anode materials to achieve upcycling-recovery of spent cathodes. Herein, sodium diethyldithiocarbamate (DDTC-Na) was utilized as a metal capture agent, and the leached Co ions could be complexed with the sulfhydryl functional group (–SH), resulting in the formation of DDTC-Co. In the molten salt, hexagonal-prism-like Co1-xS@N,S co-doped carbon composites could be derived from DDTC-Co. When used as the anode for Li ion storage, the as-fabricated composites displayed considerable electrochemical performance. In particular, tailoring of the carbonization temperature resulted in the DDTC-derived carbon coated showing different conductive traits, leading to diverse cycling stability. A detailed investigation of the physical–chemical and electrochemical properties was carried out.

Fig. 1A illustrates the detailed steps of the spent LiCoO₂ (LCO) upcycling process. Firstly, spent LCO was soaked in an HCl solution, and through the chemical reaction of LCO and H⁺ ions, all the Co ions could be collected in the solution, which is shown in Fig. 1B1. Later, as shown in Fig. 1B2, the as-prepared Co-rich solution was added to a DDTC solution, and Co–S bonds were constructed through the combination of –SH and Co²⁺ ions, resulting in the formation of DDTC-Co complexes. As shown in Fig. 1B3 and B4, through the sedimentation effect, the as-prepared DDTC-Co could be gathered in the bottle of the solution, and the powder-like DDTC-Co precursor was obtained after the drying process. Through the addition of molten salt, slight melting was triggered on the surface of the salt particles, facilitating the transformation of the precursors into carbon nanostructures. The as-obtained DDTC-Co precursors were mixed with Na₂SO₄ for further growth and carbonization process, and the samples prepared at 600 °C were named LCO6-CoS@NSC. Additionally, to explore the effect of the sintering temperature on the spent samples, a sample was processed at 500 °C and named LCO5-CoS@NSC; and samples utilizing CoCl₂ as the Co source were obtained at 500 °C and 600 °C and named CoCl5-CoS@NSC and CoCl6-CoS@NSC, respectively.

Fig. 1C compares the XRD patterns of the as-fabricated samples, which illustrate their diverse crystallinity. Comparing the samples prepared at 500 °C (including CoCl5-CoS@NSC and LCO5-CoS@NSC), LCO5-CoS@NSC displayed a higher degree of
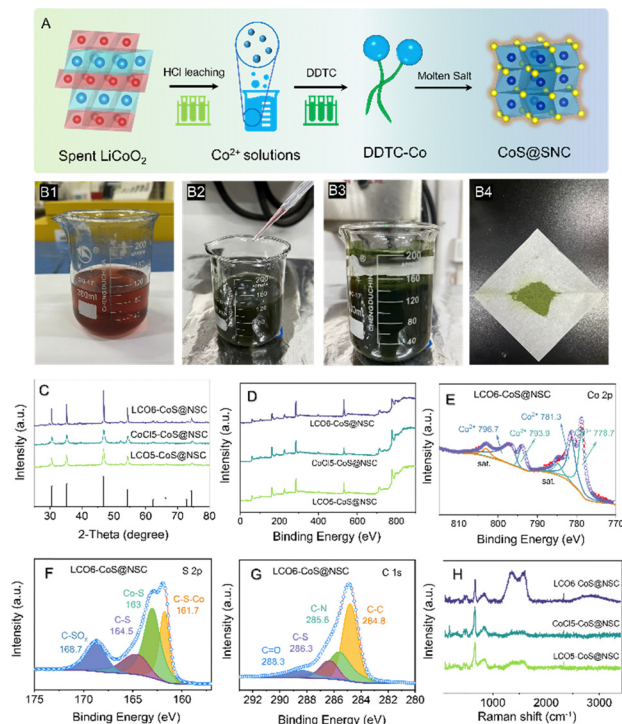
Fig. 1 (A) Fabrication steps for CoS@SNC. (B1)–(B4) Photos of the preparation steps for the DDTC-Co precursors. For the as-prepared samples: (C) XRD patterns, (D) full XPS spectra, (E) Co 2p high-resolution spectrum of LCO6-CoS@NSC, (F) S 2p high-resolution spectrum of LCO6-CoS@NSC, (G) C 1s high-resolution spectrum of LCO6-CoS@NSC. (H) Raman spectra.

crystallinity, indicating that its crystallization area was larger than that of the other samples, which was beneficial to construct the continuous ion diffusion channels. Additionally, the XRD patterns provided the phase composition. Based on the well-matching traits of the XRD patterns and the standard PDF card (PDF#42-0826), all the samples could be identified as the $Co_{1-x}S$ phase without any impurities. As denoted by the "$1 - x$" in the chemical formula provided for the standard PDF card, it could be concluded that diverse valence states of Co co-existed in the samples. Given this, XPS was utilized to analyze the element state of prepared composites. Fig. 1D illustrates the full spectra of the as-prepared samples. It should be noted that the types of elements were the same in the three samples. Fig. 1E illustrates the Co 2p high resolution XPS spectrum. The peaks located at 796.7 and 781.3 eV indicated the existence of Co^{3+}, while the peaks located at 793.9 and 778.7 eV were related to the Co^{2+} in the CoS lattice.[17,18] Thus, based on the analysis, two valence states of the element cobalt coexist synergistically, matching well with the XRD results. Fig. 1F illustrates the S 2p high-resolution spectra. The peaks located at 168.7, 164.5, 163 and 161.7 eV were related to the formation of C–SO$_x$, C–S, Co–S and C–S–Co chemical bonds.[19] The C–S bonds indicated that a fraction of the S atoms were doped into the carbon layer, which was beneficial for improving the conductivity of the as-prepared samples. Importantly, the C–S–Co chemical bonds could serve as a bridge between the carbon layer and CoS lattice, which would provide extra transportation channels for the electrons. In the C 1s high-resolution spectrum, peaks belonging to the C=O, C–S, C–N and C–C bonds could be noted at 288.3, 286.3 285.6 and 284.4 eV.[20] The formation of

C–N bonds indicated that a fraction of the N atoms were also doped into the carbon of the composite, further improving the conductivity of the as-obtained samples.[21] Fig. 1H illustrates the Raman spectra of the as-prepared samples; the peaks belonging to the carbon could clearly be divided into the G peak and D peak. Compared to the LCO6-CoS@NSC, the intensity of the G and D peak of CoCl5-CoS@NSC and LCO5-CoS@NSC were lower. Thus, it could be concluded that a low sintering temperature would lead to a large amount of H atoms remaining at the carbon layer, resulting in the inferior conductivity.

The different sintering temperatures would bring about diverse morphology traits in the resulting samples, leading to differences in their energy storage abilities. The SEM and TEM images in Fig. 2 illustrate interesting structure-evolution behaviors. As shown in Fig. 2B1–B2 and C1–C2, after the sintering process at 500 °C, a nano-dot-like structure could be noted in the SEM images, indicating that the lattice of CoS had not grown completely. As the temperature was improved to 600 °C, a series of hexagonal-like particles could be noted, as shown in Fig. 2D1, and the size of the hexagonal particles was detected to be 1809.75 nm, as shown in Fig. 2D2. Thus, as presented in Fig. 2A, the structural evolution during the sintering process could be summarized as follows. Firstly, the precursors connected with each other, and the CoS phase was generated during the 20–500 °C sintering process. However, at this stage, the growth behavior of the CoS lattice was incomplete, and the carbon layer was only partly carbonized, resulting in the inferior energy storage ability. As noted in Fig. 2E, regions with different crystal orientations can be
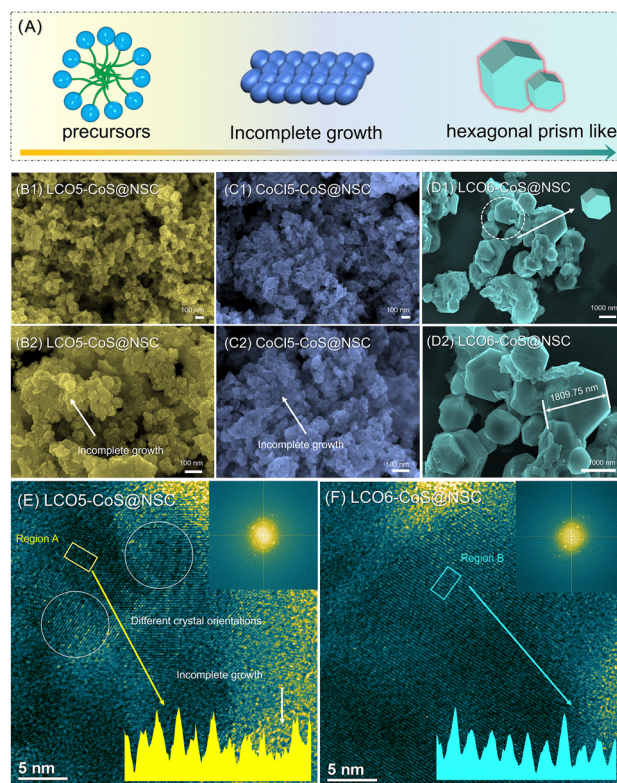

Fig. 2 (A) Morphology-evolution illustration of the as-prepared samples. SEM images of (B1)–(B2) LCO5-CoS@NSC, (C1)–(C2) CoCl5-CoS@NSC and (D1)–(D2) LCO6-CoS@NSC. TEM images of (E) LCO5-CoS@NSC and (F) LCO6-CoS@NSC.

observed in the TEM image, indicating a series of tiny unit cells that were not fully grown and fused co-existed in the 500 °C sintered samples. Additionally, the irregular crystal streaks shown in the illustration provide further evidence of incomplete grain growth at this stage. As shown in Table S1 (ESI†), from the ICP analysis, some Al and Na ions were present as impurities in the samples, which were derived from the Al foil and Na_2SO_4 molten salt.

In contrast, in the TEM images of LCO6-CoS@NSC, the crystal orientation was consistent across all regions, proving that 600 °C sintering process could provide enough energy for complete growth. Correspondingly, regular crystal streaks can be noted in Fig. 2F, further indicating the complete growth behavior of CoS. In summary, the sintering temperature was critical to the transition process from the precursor to the CoS@C composites, which mainly involves the completeness of the crystal growth process and the degree of carbonization of the hydrocarbon chain. Tailoring a suitable calcination temperature could ensure that the anode material that was converted from spent LCO could display better electrochemical performance.

Inspired by the attractive results of the physical–chemical properties investigation of the as-fabricated composites, exploration of their electrochemical properties was carried out, as shown in Fig. 3. Utilizing the three samples as the working electrodes and Li metal as the counter electrode, coin cells were assembled and further tested within the voltage range of 0.01–3.0 V. As illustrated in Fig. 3A, the cycling performance of the as-obtained samples was compared. At 1.0 A g^{-1}, LCO6-CoS@NSC, LCO5-CoS@NSC and CoCl5-CoS@NSC displayed an initial capacity of 889.8, 754.2 and 705.4 mA h g^{-1}, respectively, following the order LCO6-CoS@NSC > LCO5-CoS@NSC > CoCl5-CoS@NSC. It should be noted that obvious capacity-fading behaviors were observed for LCO5-CoS@NSC and CoCl5-CoS@NSC, which was related to their incomplete growth behaviors and the un-carbonized coated layer. After 200 cycles, LCO6-CoS@NSC retained a capacity of about 820.2 mA h g^{-1} with a capacity retention rate of 92.17%. As shown in Fig. S1 (ESI†), LCO6-CoS@NSC displayed considerable stability over 500 cycles. Fig. S2 (ESI†) illustrates the electrochemical performance of CoCl6-CoS@NSC. The electrochemical performance of CoCl6-CoS@NSC was similar to that of LCO6-CoS@NSC, indicating that the strategy of upcycling spent LCO into an anode was successful. Additionally, the rate capacity of the three samples is compared in Fig. 3B. At 0.2, 0.5, 1.0, 2.0 3.0 and 5.0 A g^{-1}, the capacity of LCO6-CoS@NSC was 977.4, 891.9, 845.6, 810.2, 794.9 and 760.9 mA h g^{-1}, which was higher than that of LCO5-CoS@NSC (888.9, 788.8, 720.3, 678.8, 630.1 and 568 mA h g^{-1} at 0.2, 0.5, 1.0, 2.0 3.0 and 5.0 A g^{-1}) and CoCl5-CoS@NSC (862.5, 797.5, 748, 707.8, 652.8 and 616 mA h g^{-1} at 0.2, 0.5, 1.0, 2.0 3.0 and 5.0 A g^{-1}). Furthermore, when applied as anode for SIBs, LCO6-CoS@NSC can achieve about 600 mA h g^{-1} at 1.0 C and displays considerable cycling stability (Fig. S3, ESI†). Thus, it could be concluded that composites derived from spent cathode materials could serve as anodes for LIBs and SIBs.

To probe the differences in the electrochemical properties of the three samples, the relationships between voltage and capacity were compared, as shown in Fig. 3C. It should be noted that three plateaus could be noted in the curves of LCO6-CoS@NSC. Based on previous work, the three plateaus indicated the three reactions during the charging and discharging plateaus.[22] The plateaus located at 1.0–1.5 V were related to the formation of polymer film, which could contributed to the increase in capacity.[23] However, only two plateaus could be noted for LCO5-CoS@NSC and CoCl5-CoS@NSC; the plateau corresponding to the polymer film vanished. Thus, it could be concluded that the incomplete growth behaviors with low sintering temperature would bring about the loss of the energy-storage plateaus, resulting in the decrease in capacity.

To further investigate the detailed mechanism of the sintering temperature and Li-ion storage ability, CV testing was carried out as shown in Fig. 3D1, E1 and F1. For comparison of the CV curves of the three as-obtained samples, the vertical current axis was set with a consistent range. It should be noted that the current intensity of LCO6-CoS@NSC was much larger than that of the other two samples, indicating its better electrochemical properties. Additionally, three peaks can be noted in the CV curves of LCO6-CoS@NSC, matching well with the analysis of the charging–discharging curves. In order to observe the differences in the CV maps of the three materials more intuitively, the CV maps were plotted in the form of contour maps, as shown in Fig. 3D2, E2 and F2. Compared to those of LCO6-CoS@NSC, the peaks of LCO5-CoS@NSC had half-vanished and those of CoCl5-CoS@NSC had fully vanished. Thus, a suitable sintering temperature was important for improving the capacity of the as-fabricated samples. Fig. 3H illustrates the relationship between the peak current and scan rate for the three as-prepared samples. By fitting the data to linear equations, the slope values were obtained, with the oxidation/reduction peak slopes following the
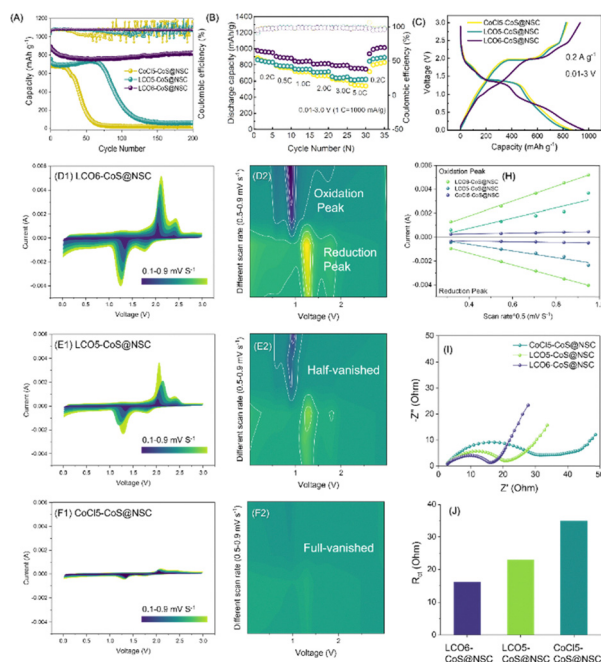

Fig. 3 For three as-fabricated samples: (A) cycling performance, (B) rate performance (C) charging/discharging curves. CV curves of (D1) LCO6-CoS@NSC, (E1) LCO5-CoS@NSC and (F1) CoCl5-CoS@NSC, and the corresponding contour maps of (D2) LCO6-CoS@NSC, (E2) LCO5-CoS@NSC and (F2) CoCl5-CoS@NSC. (H) The linear relationship between the current and scan rate. (I) Electrochemical impedance spectroscopy of the as-prepared samples and (J) the corresponding R_{ct} values.

order LCO6-CoS@NSC > LCO5-CoS@NSC > CoCl5-CoS@NSC. Using these slope values and eqn (1), the diffusion coefficient of the Li ions could be calculated. The peak current (I_p), number of electrons transferred (n), active electrode surface area (A), scan rate (ν), and concentration of Li$^+$ ions (C_{Li}^+) in the CoS lattice were defined in eqn (1). Thus, the diffusion rate of Li ions in LCO6-CoS@NSC was higher than that of other samples.[24]

$$I_p = 2.69 \times 10^5 \times n^{2/3} AD^{1/2}\nu^{1/2} \tag{1}$$

Fig. 3I presents the Nyquist plots of the as-obtained samples before the first discharge process. The Nyquist plots clearly consist of two distinct components: a semicircle in the mid-to-high frequency region and a line in the low frequency region, consistent with previous reports.[25,26] The semicircle observed in the mid-frequency region is attributed to the charge transfer resistance between the electrode material and the electrolyte. Thus, using Zview software, the R_{ct} values of the as-prepared samples were calculated and are presented in Fig. 3J; they followed the order LCO6-CoS@NSC < LCO5-CoS@NSC < CoCl5-CoS@NSC.[25,26] LCO6-CoS@NSC possessed a lower R_{ct} value than other samples, indicating that the Li transportation rate of LCO6-CoS@NSC was higher than that of the other samples.

In this study, CoS@N,S co-doped carbon composites were successfully developed using a simple upcycling approach from spent LiCoO$_2$, with a significant focus on optimizing the sintering temperature to enhance the lithium storage capability. By utilizing DDTC-Na as a capture agent, the Co ions were complexed and transformed into highly conductive CoS composites through controlled thermal treatment. The sample prepared at 600 °C (LCO6-CoS@NSC) exhibited superior crystallinity and complete carbonization compared to those prepared at lower temperatures. This well-developed crystal structure provided a continuous ion diffusion channel, resulting in a high initial capacity of 889.8 mA h g^{-1}, excellent cycling stability, and superior rate performance. In contrast, the samples sintered at 500 °C, LCO5-CoS@NSC and CoCl5-CoS@NSC, demonstrated incomplete CoS lattice growth and uncarbonized layers, leading to reduced capacity and inferior electrochemical performance. In summary, the upcycling of spent LCO into high-performance CoS@N,S co-doped carbon composites has been demonstrated to be a promising strategy for the sustainable development of anode materials for lithium-ion batteries. This work provides an effective approach for improving electrochemical properties, offering valuable insights into the design of next-generation energy storage materials.

Data availability

The data that support the findings of this study are available from the corresponding author upon reasonable request.

Conflicts of interest

There are no conflicts to declare.

References

1 W. Zhao, S. Lei, J. Li, F. Jiang, T. Wu, Y. Yang, W. Sun, X. Ji and P. Ge, *Adv. Energy Mater.*, 2024, **14**(19), 2304431.
2 Z. Zeng, W. Zhao, S. Yuan, Y. Dong, J. Zhu, F. Jiang, Y. Yang, S. Liu, L. Wang and P. Ge, *ACS Appl. Energy Mater.*, 2022, **5**, 9189–9213.
3 Y. Tang, Y. Wei, A. F. Hollenkamp, M. Musameh, A. Seeber, T. Jin, X. Pan, H. Zhang, Y. Hou, Z. Zhao, X. Hao, J. Qiu and C. Zhi, *Nano-Micro Lett.*, 2021, **13**, 178.
4 W. Zhao, S. Yuan, L. Zhang, F. Jiang, Y. Yang, G. Zou, H. Hou, P. Ge, W. Sun and X. Ji, *Energy Storage Mater.*, 2022, **45**, 1183–1200.
5 M. Hu, Z. Ju, Z. Bai, K. Yu, Z. Fang, R. Lv and G. Yu, *Small Methods*, 2019, **4**, 1900673.
6 J. B. Zhao, Y. Y. Zhang, Y. H. Wang, H. Li and Y. Y. Peng, *J. Energy Chem.*, 2018, **27**, 1536–1554.
7 Z. Zeng, Y. Dong, S. Yuan, W. Zhao, L. Wang, S. Liu, Y. Yang, P. Ge, W. Sun and X. Ji, *Energy Storage Mater.*, 2022, **45**, 442–464.
8 S. Wang, Y. Cheng, H. Xue, W. Liu, Z. Yi, L. Chang and L. Wang, *J. Mater. Chem. A*, 2021, **9**, 7838–7847.
9 Y. X. Huang, Z. H. Wang, Y. Jiang, S. J. Li, M. Wang, Y. S. Ye, F. Wu, M. Xie, L. Li and R. J. Chen, *Adv. Sci.*, 2018, **5**, 1800613.
10 S. Kang, S. Lee, H. Lee and Y.-M. Kang, *Nat. Rev. Chem.*, 2024, **8**, 587–604.
11 D. Lee, H. Kim and S. M. Jeong, *ACS Energy Lett.*, 2024, **9**(9), 4255–4264.
12 Z. Wang, L. Li, Z. Sun, P. Tang, G. Hu, J. Tan and F. Li, *Prog. Mater. Sci.*, 2024, **143**, 101247.
13 H. Yang, B. Deng, X. Jing, W. Li and D. Wang, *Waste Manage.*, 2021, **129**, 85–94.
14 Y. Gao, J. Li, J. Li, H. Xie and Y. Chen, *J. Alloys Compd.*, 2020, **845**, 156234.
15 Z. Zeng, P. Xu, J. Li, C. Yi, W. Zhao, W. Sun, X. Ji, Y. Yang and P. Ge, *Adv. Funct. Mater.*, 2023, **34**, 2308671.
16 Z. Zeng, S. Yuan, C. Yi, W. Zhao, Z. Yuan, Y. Dong, J. Zhu, Y. Yang and P. Ge, *ACS Appl. Mater. Interfaces*, 2022, **14**, 52067–52078.
17 J. Zong, F. Wang, C. Nie, M. Zhao and S. Yang, *J. Mater. Chem. A*, 2022, **10**, 10651–10661.
18 T. Zhu, W. Shen, X. Wang, Y.-F. Song and W. Wang, *Chem. Eng. J.*, 2019, **378**, 122159.
19 W. Zhao, L. Zhang, F. Jiang, X. Chang, Y. Yang, P. Ge, W. Sun and X. Ji, *J. Mater. Chem. A*, 2020, **8**, 5284–5297.
20 G. Wang, C. Chen, Z. Zeng, Y. Chen, Z. Wang, W. Zhao, S. Yuan, Y. Dong, Z. Yuan and P. Ge, *Mater. Chem. Phys.*, 2023, **310**, 128234.
21 Q. Zhang, Y. Zeng, X. Wang, L. Wang, H. Wang, J. Xiao and X. Li, *J. Alloys Compd.*, 2021, **881**, 160594.
22 J. B. G. Youngsik Kim, *J. Phys. Chem. C*, 2008, **112**, 15060.
23 Q. Wang, L. Jiao, H. Du, W. Peng, Y. Han, D. Song, Y. Si, Y. Wang and H. Yuan, *J. Mater. Chem.*, 2011, **21**, 327–329.
24 L. Zhang, W. Zhao, S. Yuan, F. Jiang, X. Chen, Y. Yang, P. Ge, W. Sun and X. Ji, *J. Energy Chem.*, 2021, **60**, 531–545.
25 C. Nithya and S. Gopukumar, *J. Mater. Chem. A*, 2014, **2**, 10516–10525.
26 M. Srout, M. Carboni, J.-A. Gonzalez and S. Trabesinger, *Small*, 2023, **19**, 2206252.